Fano line-shape control and superluminal light using cavity quantum electrodynamics with a partially transmitting element

Jiahua Li,[1,*] Rong Yu,[2,†] Jiuyang Liu,[1] Chunling Ding,[3] and Ying Wu[4,‡]

[1]*School of Physics, MOE Key Laboratory of Fundamental Physical Quantities Measurement, Huazhong University of Science and Technology, Wuhan 430074, People's Republic of China*

[2]*School of Science, Hubei Province Key Laboratory of Intelligent Robot, Wuhan Institute of Technology, Wuhan 430073, People's Republic of China*

[3]*School of Physics and Electronics, Henan University, Kaifeng 475004, People's Republic of China*

[4]*Wuhan National Laboratory for Optoelectronics and School of Physics, Huazhong University of Science and Technology, Wuhan 430074, People's Republic of China*

(Received 15 March 2016; published 9 May 2016)

We study the probe-field transmission in cavity quantum electrodynamics (cavity-QED) systems with a partially transmitting element (PTE), where the PTE is used to control and tune the amplitude of the weak probe field propagating along a single waveguide channel in the structure. We derive analytic formulas utilized to determine the transmission coefficient of the probe field within the framework of quantum optics. Using experimentally accessible parameters, it is clearly shown that the asymmetric Fano-resonance line shape can be formed and manipulated by means of the added PTE. Furthermore, we reveal that there exists superluminal light with large intensity transmission in the transport spectrum of the waveguide-coupled cavity-QED system. This superluminal-light propagation effect, which exhibits the anomalous phase shift and is characterized by the negative group delay, can be enhanced by properly choosing the system parameters. The obtained results may be used for designing switching, modulation, and sensing for nanophotonic applications and ultrafast on-chip signal processing in telecom applications.

DOI: 10.1103/PhysRevA.93.053814

I. INTRODUCTION

In quantum mechanical study of the autoionizing states of atoms, Ugo Fano [1] discovered that the quantum interference of different transition amplitudes could lead to the absorption profile that exhibits zero or minima. This phenomenon is named the so-called Fano resonance, which in general arises from quantum interference between resonant and nonresonant paths. Because of its steep asymmetric response spectra and greatly enhanced field effect, Fano resonance has many key applications in nanophotonic devices, such as optical switches, modulators, sensors, and so on. The detailed review about Fano resonance can be found in Refs. [2,3]. On the other hand, due to the fact that optical microcavities [4] have high quality factor, small mode volume, and on-chip integration in the fabrication process, the studies about the microcavity systems have emerged as an important new frontier in many discipline areas ranging from nonlinear optics [5] to cavity quantum electrodynamics (cavity-QED) [6], and in more applied domains such as ultralow-threshold lasing [7,8], coupled-resonator-induced transparency [9], photonics [10], and biological sensing [11,12], etc. Hence, considerable attention has been attracted to achieving optical Fano resonances by designing various microcavity-based devices in recent years, such as single active (i.e., gain) microcavities [13,14], two coupled whispering-gallery-mode (WGM) microcavities [15], indirectly coupled double-microcavities or multi-microcavities [16–21], microcavity optomechanics [22–24], partially blocked waveguide-coupled microcavity [25–28], involving at least two resonant modes in a single microcavity [29,30], and using a multimode waveguide as the external coupler to a single-mode or multimode microcavity [31,32], just to name a few examples.

At the same time, researches on superluminal (fast) light in recent years also have attracted a lot of interest from both theoretical and experimental views due to potential applications in quantum mutual information [33], optical gyroscope [34], optical telecommunication, and interferometry [35,36]. The term superluminal light refers to the propagation of optical signal with group velocity greater than the speed of light in vacuum or even with negative group velocity [37,38]. The anomalous dispersion results in superluminal light propagation, which in turn produces optical time advancement (negative group delay). Superluminal light has been generated by using approaches such as electromagnetically induced transparency (EIT) [39], electromagnetically induced absorption (EIA) [40], coherent population oscillation [41], stimulated Brillouin scattering [42], four-wave mixing (FWM) [43,44], spectral hole-burning [45], polarization mode coupling [34], and so on. For instance, the speed of the superluminal-light pulse had been measured in the gain-assisted atomic cesium medium [46]. In particular, the group velocity measurements of slow light and superluminality in the coherent population trapping (CPT) maser were done by directly detecting the ground state coherence of a thermal ^{87}Rb vapor, which generates the CPT or EIT phenomenon, corresponding to neither absorption or transmission [47]. On the other hand, detecting the superluminal light also is an important regime in modern physics in the context of superluminal group velocity and Einstein's special relativity theory. The superluminal light seems to contradict special relativity. However, it is now understood and accepted that

*huajia_li@163.com
†rong_yu2013@163.com
‡yingwu2@126.com

true information is not contained in the pulse peak, but instead is encoded in nonanalytical points or singularities along the wave packet [48], thereby the superluminal velocity of the signal does not violate causality [35–37,46].

By combining the above-mentioned advantages of optical microcavities and applying the theories of quantum optics (e.g., quantum coherence and interference effects), in the present work we theoretically investigate the light transmission obtained from the waveguide-coupled cavity-QED device with a partially transmitting element (PTE). This PTE can be used to control and tune the amplitude of the weak probe field propagating along a single waveguide channel in the proposed structure. We arrive at explicit analytical expressions for the amplitude or intensity transmission coefficient of the probe field within the framework of quantum optics. Using experimentally accessible parameters, it is shown that, by introducing the PTE, the symmetric Fano resonance line shape can be generated and engineered efficiently in the cavity-QED system. On the other hand, our theoretical analysis reveals that superluminal light with large intensity transmission can appear in this structure. Furthermore, the superluminal-light effect, which exhibits the anomalous phase shift and is characterized by the negative group delay, can be enhanced by suitably tuning the system parameters. These results obtained here may hold potential applications in optical switching and sensitivity-enhanced biochemical sensing.

The rest of this paper is organized as follows. The theoretical model is presented and the analytical formulas used to determine the amplitude or intensity transmission coefficient of the PTE-assisted cavity-QED system are derived in Sec. II. Assuming realistic cavity-QED parameters, optical transmission properties, i.e., asymmetric Fano-resonance line shapes, are discussed in detail in Sec. III. The transmission phase shift and negative group delay characterizing the superluminal-light effect are numerically evaluated and analyzed in Sec. IV. At the end of this section, the main advantages of applying our PTE-assisted cavity-QED scheme over other approaches are also presented. Finally, a summary is given in Sec. V.

II. THEORETICAL MODEL AND BASIC FORMULAS

Our system, depicted in Fig. 1(a), consists of a two-level quantum emitter (e.g., a quantum dot) and a single-mode microcavity adjacent to a waveguide containing a PTE. In contrast to a conventional cavity QED device, a key element, i.e., the so-called PTE, is added in the waveguide to control the amplitude of light propagating along the waveguide path. Due to the introduction of the PTE, the microcavity with resonance frequency ω_c is side-coupled to port 1 with coupling strength η_1 and to port 2 with coupling strength η_2, respectively. At the same time, the microcavity is coupled to the two-level quantum emitter with coupling strength g_c, where $|g\rangle$, $|e\rangle$, and ω_x are the ground level, excited level, and transition frequency of the quantum emitter, respectively. The electromagnetic field inside the cavity is probed by sending the continuous-wave (CW) input probe fields $S_{1\text{in}} = S_{1+}e^{-i\omega t}$ and $S_{2\text{in}} = S_{2+}e^{-i\omega t}$ with amplitudes S_{1+} and S_{2+} from the two opposite ports and measuring the output fields with amplitudes S_{1-} and S_{2-}. The squared magnitudes of these amplitudes ($|S_{1+}|^2$, $|S_{2+}|^2$, $|S_{1-}|^2$, and $|S_{2-}|^2$) correspond with the intensities. The detailed

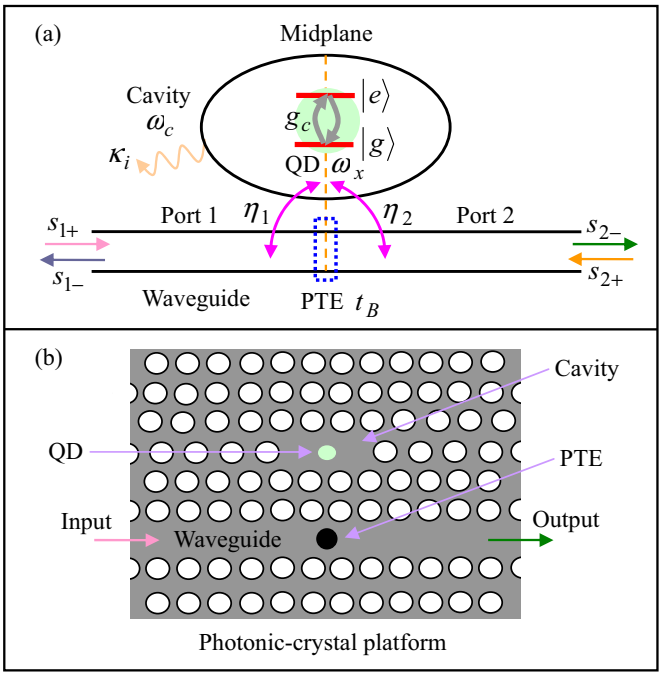

FIG. 1. (a) Schematic diagram of the proposed cavity-QED system for realizing Fano resonances and superluminal light. In contrast to a conventional cavity-QED system, an additional PTE (dotted blue square) is introduced in the waveguide, with the corresponding amplitude reflection and transmission coefficients r_B and t_B ($r_B^2 + t_B^2 = 1$). The cavity (resonance frequency ω_c and intrinsic loss rate κ_i) is side-coupled to the left waveguide (also called port 1) with coupling strength $\eta_1 = \sqrt{2\kappa_{1e}}e^{i\theta_1}$, to the right waveguide (also called port 2) with coupling strength $\eta_2 = \sqrt{2\kappa_{2e}}e^{i\theta_2}$, and to the two-level emitter (e.g., semiconductor quantum dot) with coupling strength g_c, where κ_{je} and θ_j ($j = 1,2$) are the waveguide-cavity coupling-induced loss rate and the phase factor depending on the positions of the PTE. $|g\rangle$, $|e\rangle$, and ω_x is the ground state, excited state, and transition frequency of the two-level emitter embedded in the cavity, respectively. S_{1+} and S_{2+} are the amplitudes of the two weak input fields with the same frequency ω from the two ports; S_{1-} and S_{2-} are the amplitudes of the output fields. (b) The possible realistic physical system to implement the setup (a) based on the photonic crystal membrane structure, where a linear three-holes defect cavity is formed by omitting three air holes and a W1-defect waveguide is formed by removing one array of air holes in photonic crystal structure. The PTE is generated by etching one or several BHs in the line-defect waveguide. The amplitude of the PTE, t_B, is tuned by varying the BH radius or the BH number [27,28,52]. The transmitted light intensity can be measured by using a photodetector, which is connected to both a spectrum analyzer and an oscilloscope (not shown in the sketch). QD, quantum dot.

fabrication process of similar platforms based on photonic crystal structures in Fig. 1(b) are described in Refs. [27,49]. The Hamiltonian for the investigated cavity-QED system reads

$$\begin{aligned}\mathcal{H} = {} & \hbar\omega_x\hat{\sigma}^\dagger\hat{\sigma} + \hbar\omega_c\hat{c}^\dagger\hat{c} + i\hbar g_c(\hat{c}\hat{\sigma}^\dagger - \hat{c}^\dagger\hat{\sigma}) \\ & + i\hbar\eta_1(S_{1+}e^{-i\omega t}\hat{c}^\dagger - S_{1+}^* e^{i\omega t}\hat{c}) \\ & + i\hbar\eta_2(S_{2+}e^{-i\omega t}\hat{c}^\dagger - S_{2+}^* e^{i\omega t}\hat{c}), \end{aligned} \tag{1}$$

where $\hat{\sigma} = |g\rangle\langle e|$ (its conjugate operator $\hat{\sigma}^\dagger = |e\rangle\langle g|$) is the dipole lowering (rising) operator for the two-level emitter and $\hat{c}$ (its conjugate operator $\hat{c}^\dagger$) is the annihilation (creation) operator for the cavity photon, respectively. Transforming the Hamiltonian Eq. (1) into the rotating frame at the frequency ω of the input laser based on $\mathcal{H}_0 = \hbar\omega(\hat{\sigma}^\dagger\hat{\sigma} + \hat{c}^\dagger\hat{c})$, $U(t) = e^{-i\mathcal{H}_0 t/\hbar} = e^{-i\omega t(\hat{\sigma}^\dagger\hat{\sigma}+\hat{c}^\dagger\hat{c})}$, and $\mathcal{H}_{\rm rot} = U^\dagger(t)(\mathcal{H} - \mathcal{H}_0)U(t)$, the resulting effective Hamiltonian can be derived as

$$\begin{aligned}\mathcal{H}_{\rm rot} &= \hbar\Delta_x\hat{\sigma}^\dagger\hat{\sigma} + \hbar\Delta_c\hat{c}^\dagger\hat{c} + i\hbar g_c(\hat{c}\hat{\sigma}^\dagger - \hat{c}^\dagger\hat{\sigma}) \\ &\quad + i\hbar\eta_1(S_{1+}\hat{c}^\dagger - S_{1+}^*\hat{c}) \\ &\quad + i\hbar\eta_2(S_{2+}\hat{c}^\dagger - S_{2+}^*\hat{c}),\end{aligned} \tag{2}$$

In Eq. (2), $\Delta_x = \omega_x - \omega$ and $\Delta_c = \omega_c - \omega$ are, respectively, the detunings of the input probe laser from the emitter resonant frequency ω_x and from the cavity resonance frequency ω_c.

Our analysis is based on the Heisenberg-Langevin equations that are derivable from the Hamiltonian of Eq. (2). Including losses in both the cavity and emitter, as well as cavity excitation, we apply the Heisenberg-Langevin formalism $\frac{d\hat{F}}{dt} = -\frac{i}{\hbar}[\hat{F},\mathcal{H}_{\rm rot}]$ to attain the equations of motion for the expectation values of $\hat{c}$, $\hat{\sigma}$, and $\hat{\sigma}_z \equiv \hat{\sigma}^\dagger\hat{\sigma} - \hat{\sigma}\hat{\sigma}^\dagger$ as follows:

$$\begin{aligned}\frac{dc}{dt} &= -(i\Delta_c + \kappa_{1e} + \kappa_{2e} + \kappa_i)c - g_c\sigma \\ &\quad + \eta_1 S_{1+} + \eta_2 S_{2+},\end{aligned} \tag{3}$$

$$\frac{d\sigma}{dt} = -(i\Delta_x + \gamma/2 + \gamma_d)\sigma - g_c c\sigma_z, \tag{4}$$

$$\frac{d\sigma_z}{dt} = -\gamma(\sigma_z + 1) + 2g_c(c^*\sigma + c\sigma^*), \tag{5}$$

where κ_i is the cavity intrinsic decay rate, related to the intrinsic quality factor Q_i as $\kappa_i = \omega_c/(2Q_i)$. κ_{1e} and κ_{2e} are the cavity-waveguide coupling-induced loss rates due to coupling into the two ports, related to the coupling quality factor Q_e as $\kappa_e = \kappa_{1e} + \kappa_{2e} = \omega_c/(2Q_e)$. The total cavity decay rate is $\kappa_t = \kappa_i + \kappa_e$, related to the total (loaded) quality factor Q_t as $\kappa_t = \omega_c/(2Q_t)$. Obviously, $1/Q_t = 1/Q_i + 1/Q_e$. γ and γ_d are the spontaneous emission decay rate and the dephasing rate of the emitter. When the cavity is excited by sufficiently low incoming power (i.e., a weak-field approximation), the emitter is predominantly in the ground state $|g\rangle$ in the whole process, that is, $\sigma_z \simeq -1$. Alternatively, in this condition the resonance frequency also is not perturbed by the energy build-up in the cavity.

The input field is associated with the output field and the cavity field by the input-output relation [3,50–52],

$$\begin{pmatrix} S_{1-} \\ S_{2-} \end{pmatrix} = \mathcal{M}\begin{pmatrix} S_{1+} \\ S_{2+} \end{pmatrix} + \begin{pmatrix} \eta_1 \\ \eta_2 \end{pmatrix} c, \tag{6}$$

where $\mathcal{M} = \begin{pmatrix} r_B & -it_B \\ -it_B & r_B \end{pmatrix}$ is the direct-transport scattering matrix, which stands for the direct coupling between input and output lights, in addition to the cavity-assisted photon transport. t_B (t_B^2) and r_B (r_B^2) are the corresponding amplitude (intensity) transmission and reflection coefficients of the PTE, with the relationship $t_B^2 + r_B^2 = 1$.

According to time-reversal symmetry and energy conservation [3,50–52], in the presence of the PTE we have the results $\eta_1 = \sqrt{2\kappa_{1e}}e^{i\theta_1}$ and $\eta_2 = \sqrt{2\kappa_{2e}}e^{i\theta_2}$ for the cavity-waveguide coupling strengthes, where θ_j ($j = 1,2$) is a phase factor depending on the values of t_B, r_B, κ_{1e}, and κ_{2e}. Specifically, θ_j satisfies

$$e^{i(\theta_2-\theta_1)} = it_B\sqrt{\frac{\kappa_{2e}}{\kappa_{1e}}}\frac{1}{e^{2i\theta_1} + r_B}, \tag{7}$$

$$\sin(2\theta_1) = -\frac{t_B\sqrt{4\kappa_{1e}\kappa_{2e} - (\kappa_{1e}+\kappa_{2e})^2 t_B^2}}{2\kappa_{1e}r_B}, \tag{8}$$

$$\cos(2\theta_1) = \frac{(\kappa_{2e} - \kappa_{1e})t_B^2}{2\kappa_{1e}r_B} - r_B. \tag{9}$$

With a single port excitation ($S_{2+} = 0$), the normalized amplitude transmission coefficient $t_{1\to2} = S_{2-}/S_{1+}$ of the cavity-QED system can be obtained in the steady state as

$$\begin{aligned}t_{1\to2} &= -it_B - \frac{2f_1[r_B\sqrt{\kappa_{1e}\kappa_{2e}}e^{i(\theta_2-\theta_1)} - it_B\kappa_{2e}]}{f_1 f_2 + g_c^2} \\ &= \frac{f_1 t_B(\Delta_c - i\kappa_i) - it_B g_c^2 + f_1 D}{f_1 f_2 + g_c^2},\end{aligned} \tag{10}$$

where we have defined $f_1 = i\Delta_x + \gamma/2 + \gamma_d$, $f_2 = i\Delta_c + \kappa_t$, and $D = \sqrt{4\kappa_{1e}\kappa_{2e} - (\kappa_{1e}+\kappa_{2e})^2 t_B^2}$, respectively. The intensity transmission of the device in Fig. 1 is given by $T = |t_{1\to2}|^2$.

For the structure with mirror symmetry, where the PTE in the waveguide is centered at the midplane [vertical dashed orange line in Fig. 1(a)], the condition $\kappa_{1e} = \kappa_{2e} = \kappa_e/2$ is required. As a result, the intensity transmission coefficient T can be further reduced into

$$T = \left| t_B^2 + it_B r_B - \frac{2f_1\kappa_{1e}}{f_1 f_2 + g_c^2} \right|^2. \tag{11}$$

Finally, it should be pointed out that, when the PTE and quantum emitter are absent (i.e., $t_B = 1$, $r_B = 0$, and $g_c = 0$), from Eq. (10) we have a simple form $T = \frac{\Delta_c^2 + \kappa_i^2}{\Delta_c^2 + \kappa_t^2}$, which agrees well with the results in the previous studies [53,54]. It is quite clear that the transmission spectrum exhibits a symmetric Lorentzian profile with respect to the resonance frequency $\Delta_c = 0$ at which the transmission falls to the minimum $T_{\rm min} = (\frac{\kappa_i}{\kappa_t})^2$. When only the PTE is absent (i.e., $t_B = 1$ and $r_B = 0$), the transmission reads explicitly $T = |1 - \frac{2f_1\kappa_{1e}}{f_1 f_2 + g_c^2}|^2$. Similar expressions have been derived by other groups, e.g., Refs. [55–58]. In this case, the transmission spectrum exhibits a symmetric dip-peak-dip profile.

We now use the analytical expression Eq. (10) or (11) to investigate the transmission characteristics of the coupled system. We carry out this analysis for typical parameters found experimentally in GaAs photonic crystal cavity coupled to InAs semiconductor quantum dot and a photonic crystal line-defect waveguide containing a PTE. The PTE in the waveguide is realized by etching one or several blockade-holes (BHs) [27,28]. The transmission coefficient t_B^2 of the PTE can be adjusted by changing the BH size (e.g., radius) or the BH number. Here we take $t_B^2 = 0.2$ [27,28]. The actual values of the other system parameters in relevant experiments [27,28] are chosen for the photonic crystal microcavity as the

resonance wavelength $\lambda = 1575.8$ nm, the intrinsic quality-factor $Q_i = 1.2 \times 10^4$ (corresponding to the intrinsic loss rate $\kappa_i/2\pi = c/(2\lambda Q_i) \simeq 8$ GHz, where c is the light speed in free space) [27] or $Q_i = 1.2 \times 10^5$ (corresponding to the intrinsic loss rate $\kappa_i/2\pi \simeq 0.8$ GHz) [28], and the total quality-factor $Q_t = 1.35 \times 10^3$ (corresponding to the total loss rate $\kappa_t/2\pi = c/(2\lambda Q_t) \simeq 70.5$ GHz) [27,28], respectively. The dot-cavity coupling strength is $g_c/2\pi = 20$ GHz [59,60]. The decay rate and dephasing rate of quantum dot are $\gamma/2\pi = 0.16$ GHz and $\gamma_d/2\pi = 1$ GHz [59,60], respectively. Finally, we assume the dot and cavity frequencies to be resonant, so that the detuning $\Delta_x = \Delta_c = \Delta$.

III. FANO-RESONANCE LINESHAPE CONTROL IN THE OUTPUT FIELD

In the following, we begin to examine the asymmetric Fano-resonance line shape in the output fields of the port 2 for the PTE centered at the midplane. In Fig. 2(a), we show the normalized intensity transmission spectrum for two different values of the intrinsic quality-factor Q_i as a function of the detuning Δ. As can be seen from Fig. 2(a), there exists two resonance points A and B determined by Eq. (10), at which the intensity transmission is completely suppressed. Obviously, the line shape of the intensity transmission generated in the presence of the PTE is distinctively different from conventional symmetric resonance curves like the Lorentzian-type resonance or the symmetry in the EIT windows (corresponding to $t_B^2 = 0$ or 1, as will be discussed below). One can notice that both line shapes in Fig. 2(a) clearly exhibit a characteristic of asymmetry with two zeros of transmission at the positions A and B. These are the Fano resonances. Their physical mechanism will be addressed later on in this section. In order to further show explicitly the dependency of the generated transmission spectrum on the intrinsic quality-factor Q_i and the detuning Δ, we plot, in color, the density distribution of the intensity transmission in Fig. 2(b) under the total quality-factor $Q_t = 1.35 \times 10^3$.

The appearance of the double Fano resonances mentioned above can be explained qualitatively by the interference effect. The resonance position of the first kind, denoted by A in Fig. 2(a), is due to quantum interference between the incoming light, which is used to drive the cavity mode, and the light scattered by the two-level quantum dot into the cavity mode. The interference is destructive because the light radiated by quantum dot is phase shifted by π with respect to the incoming light. Alternatively, the presence of a direct pathway (i.e., partial blockade waveguide-assisted photon transport) and an indirect pathway (i.e., cavity-mediated photon transport) gives rise to the Fano interference, thus resulting in the formation of the resonance position of the second kind, denoted by B in Fig. 2(a).

Typically the cavity intrinsic loss rate is much smaller than the external coupling loss rate, $\kappa_i \ll \kappa_e$, and we work in the mirror symmetry, $\kappa_{1e} = \kappa_{2e} = \kappa_e/2$. We expect two resonances at $\omega = \omega_c$ and at $\omega = \omega_c + \kappa_e r_B/t_B$ based on the previous discussion. According to the methods in Refs. [22,61], we examine the structure of the transmission near the resonance $\omega = \omega_c + \kappa_e r_B/t_B$ for a fixed value $\Delta_x = 0$. From the expression Eq. (10), we obtain the corresponding

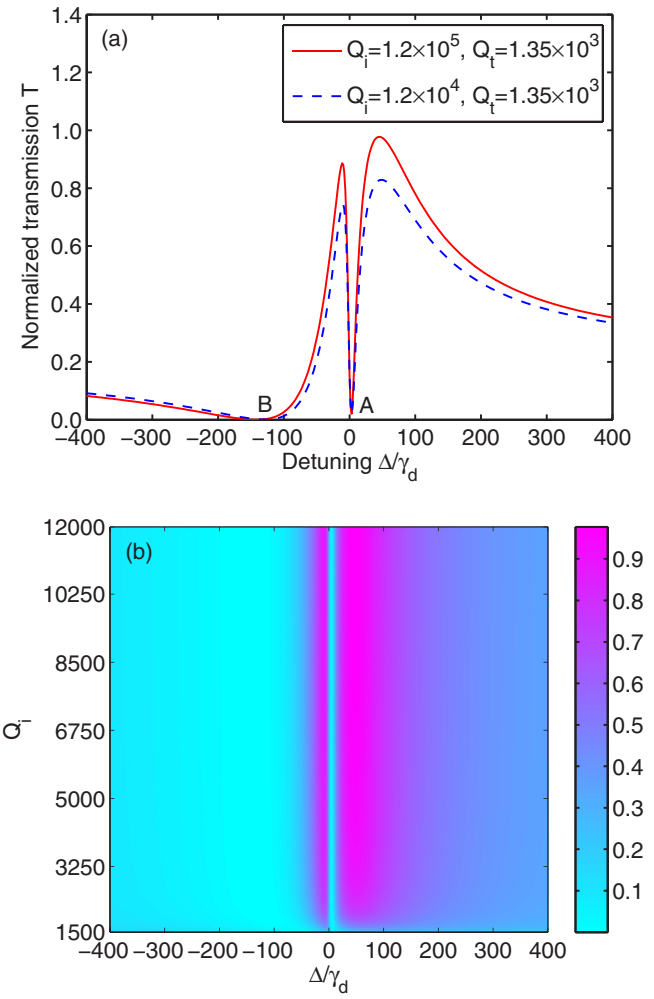

FIG. 2. (a) Calculated intensity transmission spectrum for two different values of the intrinsic quality-factor Q_i as a function of the detuning Δ when the system has mirror symmetry. (b) Density plot of the intensity transmission spectrum versus Q_i and Δ. The parameters used in the calculation are $g_c/2\pi = 20$ GHz, $t_B^2 = 0.2$, $Q_t = 1.35 \times 10^3$, $\gamma/2\pi = 0.16$ GHz, and $\gamma_d/2\pi = 1$ GHz, respectively. The resonance wavelength of the cavity mode is chosen to be 1575.8 nm here.

Fano profile

$$T \simeq t_B^2 \frac{(\epsilon + q)^2}{\epsilon^2 + 1}, \tag{12}$$

where $\epsilon = \frac{\gamma_A \Delta_c}{\gamma_A \kappa_t + g_c^2}$, $q = \frac{\gamma_A \kappa_e r_B}{(\gamma_A \kappa_t + g_c^2) t_B}$, and $\gamma_A = \gamma/2 + \gamma_d$, respectively. Obviously, from Eq. (12) the intensity transmission profile has exactly the same form as the classic profile of Fano resonance with zero at $\epsilon = -q$. The Fano factor q that determines the degree of asymmetry is related to the amplitude reflection and transmission coefficients of the PTE, r_B and t_B. First, if $t_B = 1$ or equivalently $r_B = 0$, then $q = 0$ and Eq. (12) shows a symmetric inverse Lorentzian shape. Second, if $t_B = 0$ or equivalently $r_B = 1$, then $q = \infty$ and it becomes the standard Lorentzian profile of a Breit-Wigner resonance [2]. The numerical calculations obtained directly from Eq. (10) as shown in Fig. 2 are in agreement with the above approximation formula given by Eq. (12).

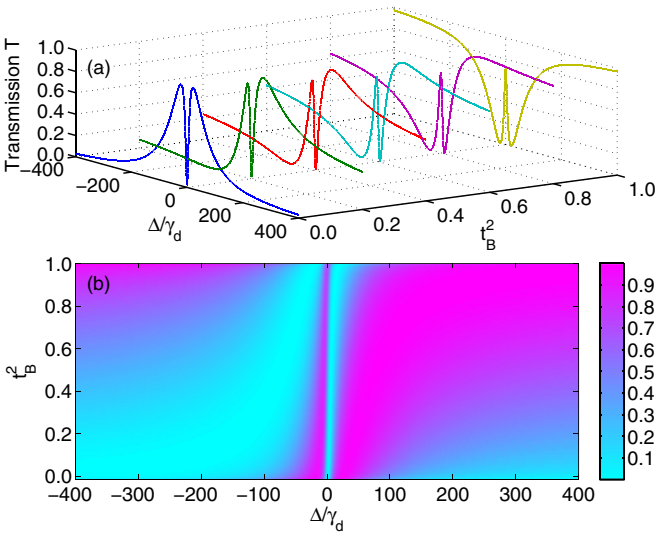

FIG. 3. (a) Calculated intensity transmission spectrum as a function of the detuning Δ for six different values of the PTE coefficient t_B^2. (b) Density plot of the intensity transmission spectrum as functions of t_B^2 and Δ. Other parameters are $g_c/2\pi = 20$ GHz, $Q_i = 1.2 \times 10^5$, $Q_t = 1.35 \times 10^3$, $\gamma/2\pi = 0.16$ GHz, and $\gamma_d/2\pi = 1$ GHz, respectively.

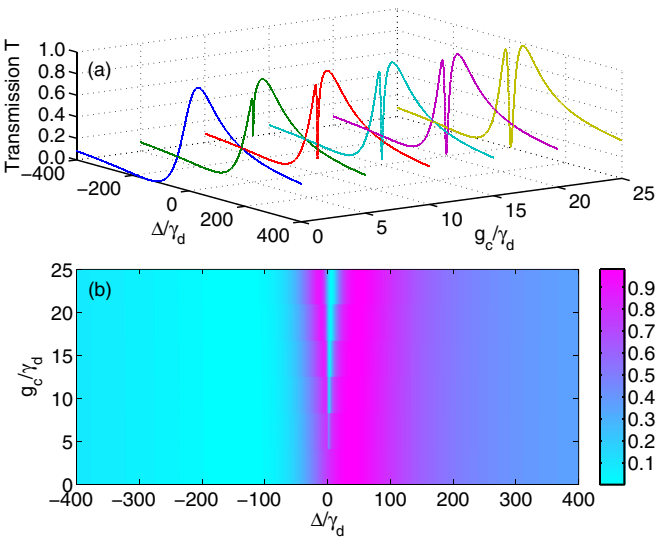

FIG. 4. (a) Calculated intensity transmission spectrum as a function of the detuning Δ for six different values of the coupling strength g_c. (b) Density plot of the intensity transmission spectrum as functions of g_c and Δ. Other parameters are $t_B^2 = 0.2$, $Q_i = 1.2 \times 10^5$, $Q_t = 1.35 \times 10^3$, $\gamma/2\pi = 0.16$ GHz, and $\gamma_d/2\pi = 1$ GHz, respectively.

In order to gain insight into the important role of the introduced PTE, we now investigate the intensity transmission spectrum by changing the intensity transmission coefficient t_B^2 of the PTE from the value of zero ($t_B^2 = 0$, complete blockade waveguide) to one ($t_B^2 = 1$, unblockade open waveguide). In Fig. 3(a), we plot the intensity transmission spectra for six different values of t_B^2 as a function of the detuning Δ. It can be seen from the curve for the case $t_B^2 = 0$ that the line shape of the resonance of the first kind is characterized by symmetry because the only path from input to output is via the cavity and the Fano resonance of the second kind disappears. Similarly, in the particular case where $t_B^2 = 1$, the line shape of the resonance of the first kind exhibits the symmetric dipole-induced transparency (DIT) evidenced by Waks *et al.* [57], since the waveguide is open and the Fano resonance of the second kind diminishes. However, for the other four cases that $t_B^2 = 0.2$, 0.4, 0.6, and 0.8 (partial blockade), there is the Fano resonance of the second kind in addition to the resonance of the first kind. Correspondingly, four out of the six line shapes clearly exhibit a characteristic of asymmetry. These are the Fano resonances. This signifies that the asymmetric line shape on both sides of the central position $\Delta = 0$ is closely associated with the Fano resonance of the second kind. If the resonance of the second kind does not exist in the structure, the asymmetric behavior of the transmission spectrum disappears. In Fig. 3(b), we show the corresponding density plot of the intensity transmission versus both t_B^2 and Δ.

Due to the existence of the quantum dot-cavity coupling in the system, the spectral structure of the output field changes in different coupling regimes. To this end, in Fig. 4(a) we plot the intensity transmission spectrum as a function of the detuning Δ for six different values of the coupling strength g_c. In Fig. 4(b), we show the density plot of the intensity transmission as functions of both g_c and Δ. One can notice that when no quantum dot is embedded in the cavity, i.e., $g_c = 0$, there only is a single Fano resonance. In contrast, when quantum dot is introduced, the change in the spectral shape can be observed obviously. For the small coupling strength $g_c/2\pi = 5$ GHz, one weak resonance occurs at $\Delta \simeq 0$ in addition to the main resonance of the second kind. As the value of g_c increases from $2\pi \times 5$ GHz to $2\pi \times 25$ GHz, the asymmetric spectral shape on both sides of the resonance dip $\Delta \simeq 0$ is gradually enhanced. It has been shown that the dot can be precisely localized at the electric field maximum of a photonic crystal cavity mode and a very strong coupling strength (about $2\pi \times 30$ GHz) can be obtained experimentally [62]. The above phenomenon can be understood in the following way. The quantum dot resonantly coupled to the cavity causes a totally destructive interference to the cavity mode. Therefore, the frequency of the cavity is split into two branches [see Fig. 4(a)] just as the energy splitting appears in the atomic level [63].

IV. TRANSMISSION PHASE SHIFT AND NEGATIVE GROUP DELAY

In what follows, we apply the formula developed in the previous section to characterize the superluminal-light effect in the system. From the expression of $t_{1\to2}$ [Eq. (10)], the transmission phase shift is given by

$$\phi = \arg(t_{1\to2}), \tag{13}$$

where "arg" denotes the argument of the amplitude transmission and $t_{1\to2} = |t_{1\to2}|e^{i\theta}$. Another interesting quantity is the first derivative of ϕ with respect to the probe frequency ω, which is related to the delay time. To this end, based on Eq. (13), the corresponding group delay can be defined as

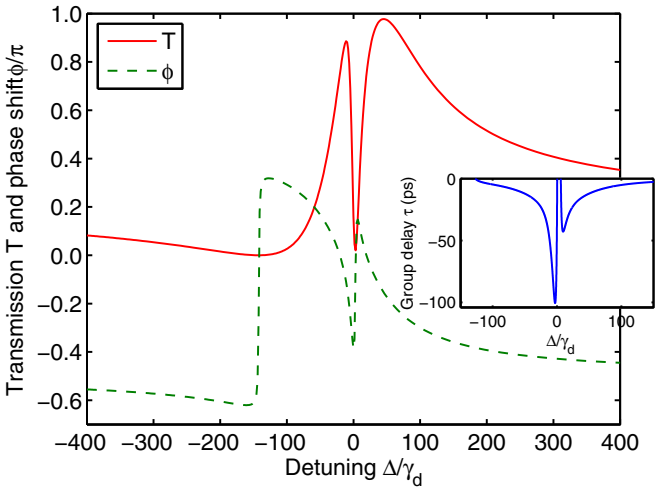

FIG. 5. Calculated transmission T (solid curve) and phase shift ϕ (dashed curve, normalized by π) as a function of the frequency detuning Δ. The inset shows the corresponding group delay τ as a function of Δ. The parameters of system are $g_c/2\pi = 20$ GHz, $t_B^2 = 0.2$, $Q_i = 1.2 \times 10^5$, $Q_t = 1.35 \times 10^3$, $\gamma/2\pi = 0.16$ GHz, and $\gamma_d/2\pi = 1$ GHz, respectively.

[64,65]

$$\tau = \frac{\partial \phi}{\partial \omega}. \tag{14}$$

We numerically evaluate Eqs. (13) and (14) to achieve the transmission phase shift and group delay of the system. The corresponding results are shown in Figs. 5–7. The red solid line in Fig. 5 depicts the intensity transmission spectrum of the waveguide-coupled cavity-QED system. It can be seen from the curve that the transmission spectrum exhibits double transparency peaks and is asymmetric with respect to the resonance point $\Delta = 0$. Alternatively, a deep single dip in the transmission line shape distinctively appears at the resonance point $\Delta = 0$. Here, for convenience we term the corresponding transparency peaks or windows as the first and second ones from left to right in the figure. As shown in Fig. 5, the second transparency window is wider than the first transparency window. At the same time, the second transmission peak is somewhat higher than the first transmission peak. The corresponding transmission phase shift, normalized by π, for the present coupled system are shown in the green dashed line of Fig. 5. Interestingly, strong anomalous dispersion is observed to accompany the two EIT-like windows, which can result in a negative group delay (see the inset of Fig. 5), i.e., the so-called superluminal light.

It should be pointed out that, in all the preceding analysis in Figs. 2–5, we focus on the structure with mirror symmetry, where the PTE in the waveguide is centered at the midplane [vertical dashed orange line in Fig. 1(a)], and the condition $\kappa_{1e} = \kappa_{2e} = \kappa_e/2$ is required. Now we will turn to discuss the structure with broken symmetry, where the PTE has an offset with respect to the midplane and both κ_{1e} and κ_{2e} can be different, i.e., $\kappa_{1e} \neq \kappa_{2e}$. As shown in Ref. [51], the ratio between κ_{1e} and κ_{2e} is constrained as follows by the direct process of the photon transport: $\frac{1-r_B}{1+r_B} \leqslant \frac{\kappa_{1e}}{\kappa_{2e}} \leqslant \frac{1+r_B}{1-r_B}$. As a result, a larger reflection coefficient r_B can arrive at a larger

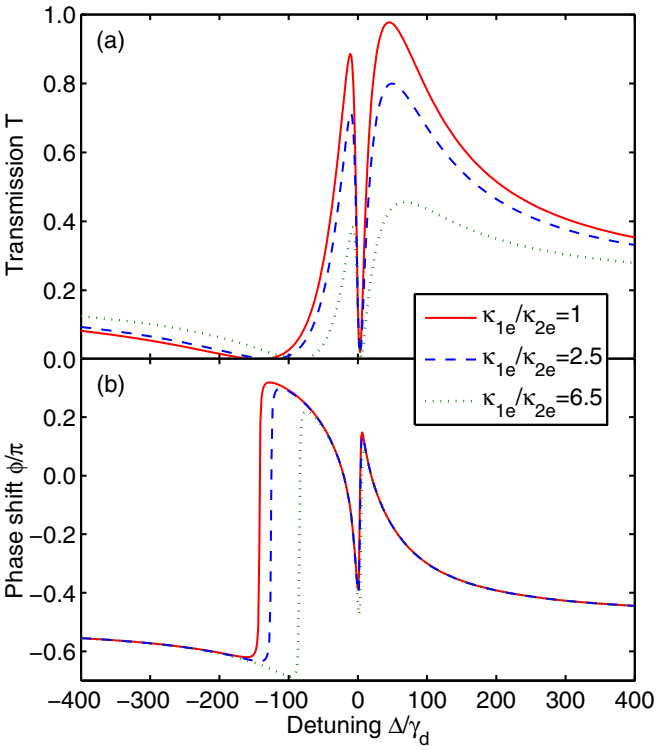

FIG. 6. Calculated transmission T [panel (a)] and phase shift ϕ [panel (b)] as a function of the frequency detuning Δ when the PTE has an offset with respect to the midplane. The parameters of system are $g_c/2\pi = 20$ GHz, $t_B^2 = 0.2$, $Q_i = 1.2 \times 10^5$, $Q_t = 1.35 \times 10^3$, $\gamma/2\pi = 0.16$ GHz, and $\gamma_d/2\pi = 1$ GHz, respectively.

ratio. As an example, when taking $t_B^2 = 0.2$ in our analysis, we have the range: $0.06 \leqslant \kappa_{1e}/\kappa_{2e} \leqslant 17.94$. In Figs. 6(a) and 6(b), we plot the intensity transmission spectrum and phase shift of the system as a function of the detuning Δ for three values of the ration κ_{1e}/κ_{2e} by shifting the PTE toward port 1 (corresponding to the ratio $\kappa_{1e}/\kappa_{2e} > 1$) [52]. It is clearly seen that a lower intensity transmission of the device is obtained when adopting the structure with broken symmetry, as compared with that of the mirror symmetry (see the red solid line of Fig. 6). This is due to the fact that only smaller energy can be coupled into the cavity. The spectral shape of the phase shift almost keeps unchange except for the contraction of the wing on the left side.

Finally, we discuss the influences of the ratio κ_{1e}/κ_{2e}, the PTE transmission coefficient t_B^2, and the dot-cavity coupling strength g_c on the group delay. The computed results are shown in Fig. 7. Specifically, in Fig. 7(a) we show the minimum negative group delay $\tau_{\min}$ as a function of the ratio κ_{1e}/κ_{2e} at $g_c/2\pi = 20$ GHz and $t_B^2 = 0.2$. It is seen from the curve that $\tau_{\min}$ decreases slowly with increasing κ_{1e}/κ_{2e}. Physically, in this situation, the excitation of the cavity is larger when the laser is injected from the port 1 since the coupling rate κ_{1e} between the input port and cavity is stronger than κ_{2e} due to the interference effects [28], which explains the enhancement in the group delay characteristic. Note that the group delay $\tau_{\min} < 0$, and the smaller the group delay $\tau_{\min}$ is, the faster the light is. Figure 7(b) displays the minimum negative group delay $\tau_{\min}$ as a function of the PTE coefficient t_B^2 at $g_c/2\pi = 20$ GHz

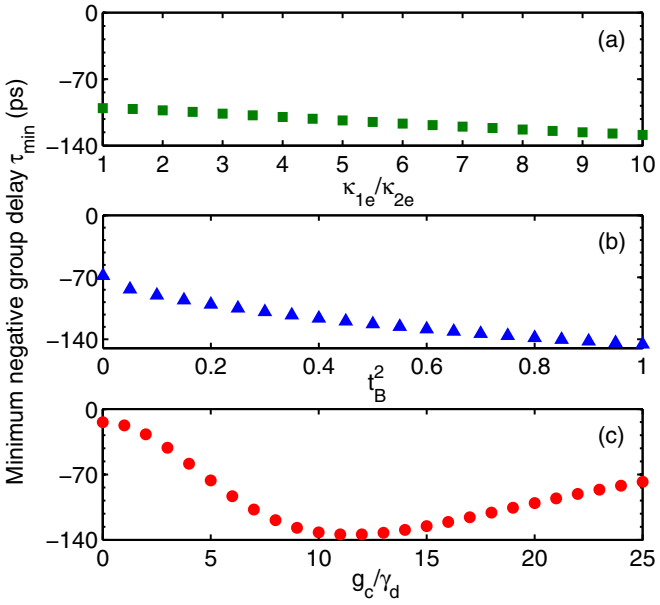

FIG. 7. (a) Minimum negative group delay $\tau_{\min}$ versus the ratio κ_{1e}/κ_{2e} at $g_c/2\pi = 20$ GHz and $t_B^2 = 0.2$. (b) Minimum negative group delay $\tau_{\min}$ versus the PTE coefficient t_B^2 at $g_c/2\pi = 20$ GHz and $\kappa_{1e}/\kappa_{2e} = 1$. (c) Minimum negative group delay $\tau_{\min}$ versus the coupling strength g_c at $t_B^2 = 0.2$ and $\kappa_{1e}/\kappa_{2e} = 1$. Other parameters for all figures are $Q_i = 1.2 \times 10^5$, $Q_t = 1.35 \times 10^3$, $\gamma/2\pi = 0.16$ GHz, and $\gamma_d/2\pi = 1$ GHz, respectively.

and $\kappa_{1e}/\kappa_{2e} = 1$. As shown in Fig. 7(b), similar characteristics as in Fig. 7(a) can be observed with t_B^2 increasing. Figure 7(c) shows the dependencies of the minimum negative group delay $\tau_{\min}$ on the coupling strength g_c at $t_B^2 = 0.2$ and $\kappa_{1e}/\kappa_{2e} = 1$. It is found from Fig. 7(c) that $\tau_{\min}$ decreases with increasing g_c until $g_c = 2\pi \times 10$ GHz, and then increases gradually due to the strong coupling.

Before ending this section, we give a discussion on the main advantages (including the novelty and new phenomena in our findings) of applying our PTE-assisted waveguide-cavity-QED scheme over other approaches as follows. First, it should be emphasized that the asymmetric Fano resonance and superluminal-light effect can occur in a low-Q microcavity (here Q refers to total quality-factor Q_t), that is to say, a weak-coupling regime, where the coupling strength g_c between the dipole emitter and the cavity is smaller than the cavity decay rate κ_t ($g_c \ll \kappa_t$). Hence, our design relaxes the requirements in the fabrication process and allows a more practical parameter range for solid-state materials. Second, the transmission spectrum and the dispersive phase response can be controlled by the PTE. Note that in the photonic crystal structure, the PTE transmittance (i.e., t_B^2 or r_B^2) can be well tuned by simply varying the BH size or the BH number [see Fig. 1(b)]. Thereby, the asymmetry of the Fano resonance and the slopes of phase variation are easily adjustable. Third, the double-frequency Fano resonances can be generated in this scheme as shown in the positions A and B of Fig. 2(a), which originate from two different mechanisms. This is different from the Fano effect in the previous waveguide-cavity structures [27,28]. Compared with the conventional single Fano resonance, the double Fano resonances are used to simultaneously achieve controllable spectral line-shaping at different frequencies, which is important for double-wavelength sensing. At the same time, it is possible to create double EIT-like windows in such coupled system, which simultaneously support negative group velocities (i.e., fast light) for two input signals at different frequencies as shown in Fig. 5. The double-frequency transparency of the input light expands the frequency range of EIT and may improve the controllability of EIT, which provides an easy way to achieve integrated photonic devices on a chip for applications requiring EIT and fast-light effects.

V. CONCLUSION

In summary, we theoretically have investigated the PTE-induced Fano line-shape control and superluminal-light propagation in the waveguide-coupled cavity-QED systems. There are two main results of this study. First, our theoretical analysis shows that the PTE placed in the waveguide and the quantum emitter confined in the cavity play a key role in the evolution and modification of the asymmetric Fano-resonance lineshape. Second, the enhanced negative group delay τ, accompanied with high-intensity transmission in the output port 2, can be obtained by properly adjusting the system parameters. We also present the on-chip experimental platform based on photonic crystal nanostructure that can be used to implement our proposal. The proposed theory can be extended to cavity optomechanical system [66–68]. Our results in this study provide potential applications not only in ultrafast on-chip signal processing but also in optical switching and high-sensitivity biochemical sensing.

Finally, it is pointed out that a few natural extensions to the present investigation can be envisaged and also would be interesting. For example, is it possible to induce "multiple" interferences? What if, for example, two PTEs are considered? Is it possible to induce something like Ramsey-Fano interferences [69]? According to our preliminary analysis, these multiple interferences like Ramsey-Fano interferences may be realized when two or more PTEs are applied. Addressing and answering the above-mentioned issues is beyond the scope of this paper and these interesting issues will be taken into account more systematically in future study.

ACKNOWLEDGMENTS

We thank the anonymous referees for their constructive comments and suggestions to improve our paper. We also are grateful to Xiao-Xue Yang and Xin-You Lü for useful advice and discussion in preparing the manuscript. J.L. and Y.W. are supported in part by the National Basic Research Program of China (973 Program) under Contract No. 2012CB922103 and the National Natural Science Foundation of China (NSFC) under Grants No. 11375067 and No. 11574104. R.Y. is supported by the NSFC under Grant No. 11505131 and the Youth Fund Project of Wuhan Institute of Technology under Grant No. Q201408. C.D. is supported by the NSFC under Grants No. 11447107 and No. U1504111, as well as the Doctoral Foundation of the Ministry of Education of China under Grant No. 20134103120005.

[1] U. Fano, Effects of configuration interaction on intensities and phase shifts, Phys. Rev. **124** 1866 (1961).

[2] A. E. Miroshnichenko, S. Flach, and Y. S. Kivshar, Fano resonances in nanoscale structures, Rev. Mod. Phys. **82**, 2257 (2010).

[3] W. Zhou, D. Zhao, Y. C. Shuai, H. Yang, S. Chuwongin, A. Chadha, J. H. Seo, K. X. Wang, V. Liu, Z. Ma, and S. Fan, Progress in 2 D photonic crystal Fano resonance photonics, Prog. Quantum Electron. **38** 1 (2014).

[4] K. J. Vahala, Optical microcavities, Nature (London) **424**, 839 (2003).

[5] R. K. Chang and A. J. Campillo, *Optical Processes in Microcavities* (World Scientific, Singapore, 1996).

[6] H. J. Kimble, Strong interactions of single atoms and photons in cavity QED, Phys. Scr., T **76**, 127 (1998).

[7] L. Yang, T. Carmon, B. Min, S. M. Spillane, and K. J. Vahala, Erbium-Doped and Raman Microlasers on a Silicon Chip Fabricated by the Sol-Gel Process, Appl. Phys. Lett. **86**, 091114 (2005).

[8] Y. Wu, X. Yang, and P. T. Leung, Theory of microcavity-enhanced Raman gain, Opt. Lett. **24**, 345 (1999).

[9] D. D. Smith, H. Chang, K. A. Fuller, A. T. Rosenberger, and R. W. Boyod, Coupled-resonator-induced transparency, Phys. Rev. A **69**, 063804 (2004).

[10] V. S. Ilchenko and A. B. Matsko, Optical resonators with whispering-gallery modes-part I: basics, IEEE J. Sel. Top. Quantum Electron. **12**, 15 (2006).

[11] A. M. Armani, R. P. Kulkarni, S. E. Fraser, R. C. Flagan, and K. J. Vahala, Label-free, single-molecule detection with optical microcavities, Science **317**, 783 (2007).

[12] J. Wiersig, Sensors operating at exceptional points: General theory, Phys. Rev. A **93**, 033809 (2016).

[13] F. Lei, B. Peng, Ş. K. Özdemir, G. L. Long, and L. Yang, Dynamic Fano-Like Resonances in Erbium-Doped Whispering-Gallery-Mode Microresonators, Appl. Phys. Lett. **105**, 101112 (2014).

[14] L. He, Ş. K. Özdemir, Y.-F. Xiao, and L. Yang, Gain-induced evolution of mode splitting spectra in a high-Q active microresonator, IEEE J. Quantum Electron. **46**, 1626 (2010).

[15] B. Peng, S. K. Ozdemir, W. Chen, F. Nori, and L. Yang, What is and what is not electromagnetically induced transparency in whispering-gallery microcavities, Nature Commun. **5**, 5082 (2014).

[16] X. D. Yang, C. Husko, C. W. Wong, M. B. Yu, and D.-L. Kwong, Observation of Femtojoule Optical Bistability Involving Fano Resonances in High-Q/V_m Silicon Photonic Crystal Nanocavities, Appl. Phys. Lett. **91**, 051113 (2007).

[17] Y. Xiao, V. Gaddam, and L. Yang, Coupled optical microcavities: An enhanced refractometric sensing configuration, Opt. Express **16**, 12538 (2008).

[18] Y. Xiao, M. Li, Y. Liu, Y. Li, X. Sun, and Q. Gong, Asymmetric Fano resonance analysis in indirectly coupled microresonators, Phys. Rev. A **82**, 065804 (2010).

[19] B.-B. Li, Y.-F. Xiao, C.-L. Zou, X.-F. Jiang, Y.-C. Liu, F.-W. Sun, Y. Li, and Q. Gong, Experimental Controlling of Fano Resonance in Indirectly Coupled Whispering-Gallery Microresonators, Appl. Phys. Lett. **100**, 021108 (2012).

[20] K. Nozaki, A. Shinya, S. Matsuo, T. Sato, E. Kuramochi, and M. Notomi, Ultralow-energy and high-contrast all-optical switch involving Fano resonance based on coupled photonic crystal nanocavities, Opt. Express **21**, 11877 (2013).

[21] S. Longhi, Tunable dynamic Fano resonances in coupled-resonator optical waveguides, Phys. Rev. A **91**, 063809 (2015).

[22] K. Qu and G. S. Agarwal, Fano resonances and their control in optomechanics, Phys. Rev. A **87**, 063813 (2013).

[23] J. Fan, C. Huang, and L. Zhu, Optomechanical nonlinearity enhanced optical sensors, Opt. Express **23**, 2973 (2015).

[24] R. Madugani, Y. Yang, J. M. Ward, V. H. Le, and S. N. Chormaic, Optomechanical Transduction and Characterization of a Silica Microsphere Pendulum Via Evanescent Light, Appl. Phys. Lett. **106**, 241101 (2015).

[25] S. Fan, Sharp Asymmetric Line Shapes in Side-Coupled Waveguide-Cavity Systems, Appl. Phys. Lett. **80**, 908 (2002).

[26] M. Heuck, P. T. Kristensen, Y. Elesin, and J. Mørk, Improved switching using Fano resonances in photonic crystal structures, Opt. Lett. **38**, 2466 (2013).

[27] Y. Yu, M. Heuck, H. Hu, W. Xue, C. Peucheret, Y. Chen, L. K. Oxenløwe, K. Yvind, and J. Mørk, Fano Resonance Control in a Photonic Crystal Structure and its Application to Ultrafast Switching, Appl. Phys. Lett. **105**, 061117 (2014).

[28] Y. Yu, Y. Chen, H. Hu, W. Xue, K. Yvind, and J. Mork, Nonreciprocal transmission in a nonlinear photonic-crystal Fano structure with broken symmetry, Laser & Photon. Rev. **9**, 241 (2015).

[29] Y.-F. Xiao, L. He, J. Zhu, and L. Yang, Electromagnetically Induced Transparency-Like Effect in a Single Polydimethylsiloxane-Coated Silica Microtoroid, Appl. Phys. Lett. **94**, 231115 (2009).

[30] J. D. Franson and S. M. Hendrickson, Optical transparency using interference between two modes of a cavity, Phys. Rev. A **74**, 053817 (2006).

[31] A. Chiba, H. Fujiwara, J. I. Hotta, S. Takeuchi, and K. Sasaki, Fano Resonance in a Multimode Tapered Fiber Coupled with a Microspherical Cavity, Appl. Phys. Lett. **86**, 261106 (2005).

[32] W. Suh, Z. Wang, and S. Fan, Temporal coupled-mode theory and the presence of nonorthogonal modes in lossless multimode cavities, IEEE J. Quantum Electron. **40**, 1511 (2004).

[33] J. B. Clark, R. T. Glasser, Q. Glorieux, U. Vogl, T. Li, K. M. Jones, and P. D. Lett, Quantum mutual information of an entangled state propagating through a fast-light medium, Nature Photon. **8**, 515 (2014).

[34] David D. Smith, H. Chang, Krishna Myneni, and A. T. Rosenberger, Fast-light enhancement of an optical cavity by polarization mode coupling, Phys. Rev. A **89**, 053804 (2014).

[35] L. Thevenaz, Slow and fast light in optical fibers, Nat. Photon. **2**, 474 (2008).

[36] R. W. Boyd, Slow and fast light: Fundamentals and applications, J. Mod. Opt. **56**, 1908 (2009).

[37] L. Brillouin, *Wave Propagation and Group Velocity* (Academic, New York, 1960).

[38] A. M. Akulshin and R. J. McLean, Fast light in atomic media, J. Opt. **12**, 104001 (2010).

[39] H. Kang, G. Hernandez, and Y. Zhu, Superluminal and slow light propagation in cold atoms, Phys. Rev. A **70**, 011801(R) (2004).

[40] M. Mirhosseini, G. Viza, O. S. Magaña-Loaiza, M. Malik, J. C. Howell, and R. W. Boyd, Weak-value amplification of the fast-light effect in rubidium vapor, arXiv:1412.3019.

[41] F. Arrieta-Yáñez, O. G. Calderón, and S. Melle, Slow and fast light based on coherent population oscillations in erbium-doped fibres, J. Opt. **12**, 104002 (2010).

[42] M. González-Herráez, K.-Y. Song, and L. ThÉvenaz, Optically Controlled Slow and Fast Light in Optical Fibers Using Stimulated Brillouin Scattering, Appl. Phys. Lett. **87**, 081113 (2005).

[43] Ryan T. Glasser, Ulrich Vogl, and Paul D. Lett, Stimulated Generation of Superluminal Light Pulses via Four-Wave Mixing, Phys. Rev. Lett. **108**, 173902 (2012).

[44] Y. Wu, Two-color ultraslow optical solitons via four-wave mixing in cold-atom media, Phys. Rev. A **71**, 053820 (2005).

[45] R. P. Rajan, A. Rebane, and H. Riesen, Rapid switching between slow and fast light by frequency-modulated transient spectral hole-burning, J. Opt. Soc. Am. B **32**, 2019 (2015).

[46] L. J. Wang, A. Kuzmich, and A. Dogarlu, Gain-assisted superluminal light propagation, Nature (London) **406**, 277 (2000).

[47] A. Godone, F. Levi, and S. Micalizio, Slow light and superluminality in the coherent population trapping maser, Phys. Rev. A **66**, 043804 (2002).

[48] R. Suzuki and M. Tomita, Causal propagation of nonanalytical points in fast- and slow-light media, Phys. Rev. A **88**, 053822 (2013).

[49] R. Bose, D. Sridharan, H. Kim, G. S. Solomon, and E. Waks, Low-Photon-Number Optical Switching with a Single Quantum Dot Coupled to a Photonic Crystal Cavity, Phys. Rev. Lett. **108**, 227402 (2012).

[50] S. H. Fan, W. Suh, and J. D. Joannopoulos, Temporal coupled-mode theory for the Fano resonance in optical resonators, J. Opt. Soc. Am. A **20**, 569 (2003).

[51] K. X. Wang, Z. Yu, S. Sandhu, and S. Fan, Fundamental bounds on decay rates in asymmetric single-mode optical resonators, Opt. Lett. **38**, 100 (2013).

[52] Y. Yu, H. Hu, L. K. Oxenløwe, K. Yvind, and J. Mork, Ultrafast all-optical modulation using a photonic-crystal Fano structure with broken symmetry, Opt. Lett. **40**, 2357 (2015).

[53] Q. Li, T. Wang, Y. Su, M. Yan, and M. Qiu, Coupled mode theory analysis of mode-splitting in coupled cavity system, Opt. Express **18**, 8367 (2010).

[54] J. Li, R. Yu, C. Ding, and Y. Wu, $\mathcal{PT}$-symmetry-induced evolution of sharp asymmetric line shapes and high-sensitivity refractive index sensors in a three-cavity array, Phys. Rev. A **93**, 023814 (2016).

[55] A. Auffèves-Garnier, C. Simon, J.-M. Gérard, and J.-P. Poizat, Giant optical nonlinearity induced by a single two-level system interacting with a cavity in the Purcell regime, Phys. Rev. A **75**, 053823 (2007).

[56] J. T. Shen and S. Fan, Theory of single-photon transport in a single-mode waveguide. I. Coupling to a cavity containing a two-level atom, Phys. Rev. A **79**, 023837 (2009).

[57] E. Waks and J. Vučković, Dipole Induced Transparency in Drop-Filter Cavity-Waveguide Systems, Phys. Rev. Lett. **96**, 153601 (2006).

[58] S. Hughes and C. Roy, Nonlinear photon transport in a semiconductor waveguide-cavity system containing a single quantum dot: Anharmonic cavity-QED regime, Phys. Rev. B **85**, 035315 (2012).

[59] A. Majumdar, M. Bajcsy, and J. Vučković, Probing the ladder of dressed states and nonclassical light generation in quantum-dot-cavity QED, Phys. Rev. A **85**, 041801(R) (2012).

[60] A. Faraon, A. Majumdar, H. Kim, P. Petroff, and J. Vučković, Fast Electrical Control of a Quantum Dot Strongly Coupled to a Photonic-Crystal Cavity, Phys. Rev. Lett. **104**, 047402 (2010)

[61] L. Schwarz, H. Cartarius, G. Wunner, W. D. Heiss, and J. Main, Fano resonances in scattering: An alternative perspective, Eur. Phys. J. D **69**, 196 (2015).

[62] D. Englund, A. Majumdar, M. Bajcsy, A. Faraon, P. Petroff, and J. Vučković, Ultrafast Photon-Photon Interaction in a Strongly Coupled Quantum Dot-Cavity System, Phys. Rev. Lett. **108**, 093604 (2012).

[63] M. O. Scully and M. S. Zubairy, *Quantum Optics* (Cambridge University Press, Cambridge, 1997).

[64] V. S. C. Manga Rao and S. Hughes, Single quantum dots for slow and fast light in a planar photonic crystal, Opt. Lett. **32**, 304 (2007).

[65] Y. Huo, S. Sandhu, J. Pan, N. Stuhrmann, M. L. Povinelli, J. M. Kahn, J. S. Harris, M. M. Fejer, and S. Fan, Experimental demonstration of two methods for controlling the group delay in a system with photonic-crystal resonators coupled to a waveguide, Opt. Lett. **36**, 1482 (2011).

[66] M. Aspelmeyer, T. J. Kippenberg, and F. Marquardt, Cavity optomechanics, Rev. Mod. Phys. **86**, 1391 (2014).

[67] X. Sun, X. Zhang, M. Poot, C. Xiong, and H. X. Tang, A Superhigh-Frequency Optoelectromechanical System Based on a Slotted Photonic Crystal Cavity, Appl. Phys. Lett. **101**, 221116 (2012).

[68] X. Sun, J. Zheng, M. Poot, C. W. Wong, and H. X. Tang, Femtogram doubly clamped nanomechanical resonators embedded in a high-Q two-dimensional photonic crystal nanocavity, Nano Lett. **12**, 2299 (2012).

[69] S. Micalizio, C. E. Calosso, F. Levi, and A. Godone, Ramsey-fringe shape in an alkali-metal vapor cell with buffer gas, Phys. Rev. A **88**, 033401 (2013).